Bonding Hierarchy and Phonon Coherence Enhanced Ultralow Lattice Thermal Conductivity and Excellent Thermoelectric Properties in Cs_2TeI_6

Jing-Jing Zheng(郑晶晶)[1], Chao-jun Li(李超军)[1], Rong-Rong Ma(马荣荣)[2], Bao-Tian Wang(王保田)[3,4*], and Jiang-Jiang Ma(马江将)[2*]

[1]*Department of Physics, Taiyuan Normal University, Jinzhong 030619, China*
[2]*School of Physics and Electronics Engineering, Shanxi Normal University, Taiyuan 030031, China*
[3]*Institute of High Energy Physics, Chinese Academy of Sciences, Beijing 100049, China*
[4]*Spallation Neutron Source Science Center, Dongguan 523803, China*

(Received 11 April 2025; accepted manuscript online 9 June 2025)

Lead-free halide perovskites provide a promising solution for efficient thermoelectric materials due to their ultralow lattice thermal conductivity (κ_L). However, disadvantages such as the electrically resistive nature strongly affect their power factor. In this work, we introduced the Te-based halide perovskites thermoelectric material Cs_2TeI_6, which is already known as a promising candidate for photovoltaic applications due to its moderate band gap. Our findings reveal that Cs_2TeI_6 has an exceptionally ultralow κ_L at room temperature, reaching as low as $0.17\,W{\cdot}m^{-1}{\cdot}K^{-1}$. We found that the four-phonon scattering processes play a dominant role in suppressing the thermal transport, leading to an approximate 50% reduction in its particle-like thermal conductivity κ_p at 300 K. The ultralow κ_L can be mainly attributed to the strong discrepancy in bonding strength, which induces large anharmonicity. The flat and dense phonon dispersions result in a strong phonon scattering rate, making it easy to generate wavelike phonon tunneling. After accounting for the wavelike thermal conductivity κ_c, a nonstandard $T^{-0.30}$ temperature dependence was observed. Benefiting from the ultralow κ_L, n-type Cs_2TeI_6 is predicted to achieve an extraordinary ZT of 2.26 at 700 K. This work highlights a pathway for searching high-performance and low-cost thermoelectrics based on lead-free halide perovskites.

DOI: 10.1088/0256-307X/42/8/080703 CSTR: 32039.14.0256-307X.42.8.080703

Thermoelectric (TE) materials enable the direct interconversion of thermal energy and electricity, making them promising candidates for waste heat recovery and solid-state refrigeration.[1–4] TE conversion efficiency is quantified by the dimensionless figure of merit ZT, defined as $ZT = S^2\sigma T/(\kappa_e + \kappa_L)$, where S is the Seebeck coefficient, σ is the electrical conductivity, T is the absolute temperature, κ_e is the electrical thermal conductivity, and κ_L is the lattice thermal conductivity. To enhance TE performance, researchers have adopted several strategies to improve electrical transport properties and reduce thermal conductivity, such as band engineering and defect engineering.[5,6] However, electrical transport is generally accompanied by heat transfer. Among these parameters, κ_L is unique, as it is an independent factor that does not directly affect electrical transport. Thus, identifying materials with intrinsically low κ_L for effective heat conduction suppression has emerged as a key guiding principle in advancing TE applications.

Recently, halide perovskites have received renewed attention due to their intrinsically low κ_L.[7–9] Despite this advantage, perovskites typically exhibit poor electrical transport properties. For instance, their large band gap restricts electrical conductivity, presenting a significant challenge.[10–13] Therefore, it is crucial to discover perovskite materials that strike a balance between excellent electrical transport properties and low κ_L. Cs_2TeI_6 is a vacancy-ordered double perovskite that has garnered attention for photovoltaic and optoelectronic application due to its moderate band gap (about 1.5–1.6 eV) and high absorption coefficient.[14–18] Additionally, these characteristics align with the essential requirements for TE materials, suggesting the possibility of finely tuning electronic conductivity, thermal conductivity, and Seebeck coefficient to achieve a high ZT value.

In this Letter, we report a theoretical study on the TE properties of a promising perovskite material Cs_2TeI_6. It crystallizes in a defect variant of the ABX_3 perovskite structure. Specifically, it features a vacancy-ordered double perovskite structure, where half of the Te atoms are missing, creating vacancies that influence its properties. Figures 1(a) and 1(b) illustrate the primitive and conventional unit cells, respectively. Cs_2TeI_6 is a face-centered cubic structure with a space group $Fm\bar{3}m$ (No.225). The Cs, Te, and I atoms occupy the 8**c**, 4**a**, and 24**e** positions, with site symmetries of $\bar{4}3m$, $m\bar{3}m$, and $4mm$, respectively. The Te atoms are located at the center of discrete $[TeI_6]^{2-}$ octahedral anion clusters. The eight Cs atoms are positioned at the tetragonal interstitial sites (face-centered positions), exhibiting 12-fold coordination with I anions.

*Corresponding authors. Email: wangbt@ihep.ac.cn; majiangjiang@sxnu.edu.cn
© 2025 Chinese Physical Society and IOP Publishing Ltd. All rights, including for text and data mining, AI training, and similar technologies, are reserved.

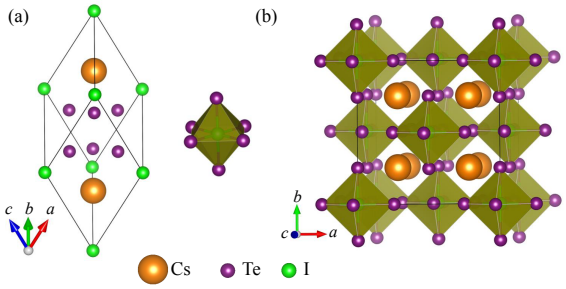

Fig. 1. Crystal structures of (a) the primitive and (b) the conventional cells for Cs_2TeI_6. The small yellow, purple, and green spheres represent Cs, Te, and I atoms, respectively. The olive-colored geometries represents the $[TeI_6]^{2-}$ octahedral anion clusters.

Table 1. The calculated lattice parameter and bond length with PBE and PBEsol functionals.

Methods	Lattice parameter (Å)	Bond length (Å)	
		I-Te	I-Cs
PBE	12.080	2.973	4.271
PBEsol	11.605	2.933	4.103
Exp.	11.589 [19]		
	11.709 [19]		
Theo.	12.066 [17]	2.98	4.27 [17]
	12.06 [21]		

This configuration essentially embeds the Cs atoms within a framework formed by the $[TeI_6]^{2-}$ octahedra.

Table 1 presents a comprehensive comparison of the lattice constants and bond lengths of Cs_2TeI_6 calculated using PBE and PBEsol functionals. The results obtained with the PBEsol functional align remarkably well with those previously reported values measured at 10 K.[19] Notably, the Cs-I bond length of 4.133 Å is significantly longer than the Te-I bond length of 2.933 Å. The isosurface of the electron localization function (ELF), as shown in Fig. S1 of the Supplementary Materials (SM), displays charge overlap between I and Te atoms, indicating the presence of covalent bonding, while the electrons surrounding the Cs atoms are relatively localized, suggesting weak interactions between Cs and its neighboring atoms. Such bonding hierarchy has also been observed in other halide perovskites, such as $Cs_3Bi_2I_6Cl_3$,[7] $Cs_3Bi_2X_9$ (X = Br, I).[20]

We investigate the mechanical and dynamical stability of Cs_2TeI_6 by calculating the elastic constants and phonon dispersion. Since Cs_2TeI_6 belongs to the cubic system, three independent elastic constants (C_{11} = 17.44 GPa, C_{12} = 9.28 GPa, and C_{44} = 7.49 GPa) are calculated to evaluate its mechanical properties. Obviously, the elastic constants satisfy the elastic stability criteria,[22] $C_{11}-C_{12} > 0$, $C_{11}+2C_{12} > 0$, and $C_{44} > 0$. Thus, Cs_2TeI_6 is mechanically stable. In addition, we perform *ab initio* molecular dynamics simulations for 10 ps to demonstrate the thermodynamic stability at 300 and 700 K, as shown in Fig. S2 of the SM. The temperature-dependent phonon dispersions are displayed in Fig. 2(a). The phonon modes do not exhibit any imaginary frequencies in the Brillouin zone, indicating the dynamical stability of Cs_2TeI_6. It is clear that the high-frequency optical modes do not change notably, while the acoustic phonon modes exhibit a pronounced hardening as temperature increases, especially in the frequency range of 1.8–3.7 meV. The low-lying optical phonons and the acoustic branches exhibit an avoided crossing behavior, as shown in Fig. S3 of the SM, due to the repulsion between two modes.[23,24] In addition, the optical modes exhibit a flat dispersion and dense distribution, indicating highly localized atomic vibrations. The flat phonon dispersions result in ultralow group velocities, as illustrated in Fig. S4(a) of the SM. Notably, in the medium-frequency region, the phonon branches are nearly horizontal, leading to group velocities almost entirely below 0.5 km/s. The low group velocity is anticipated to directly result in low κ_L. As shown in the atom-decomposed phonon density of states (PhDOS) in Fig. 2(b), the localized vibrations are predominantly attributed to the vibrations of the I and Cs atoms. This may lead to rattling vibration modes due to the weak interactions between these atoms and their surroundings.[25,26]

To elucidate the interaction of atoms, we calculated the potential energy surfaces (PES) of the nearly flat optical phonon modes at 4.46, 7.33, and 20.11 meV at Γ point, as shown in Fig. 2(c). The 10th and the 27th phonon branches predominantly represent the translational vibrations of the Cs and Te atoms at 4.46 and 20.11 meV, respectively. These vibrational modes are accompanied by the motion of I atoms, including translational or octahedral tilting vibrations. In contrast, the 16th branch at 7.33 meV corresponds to $[TeI_6]^{2-}$ octahedra tilting vibrations. The PES corresponding to these three vibrational modes show a single-well potential nature, indicating a stable crystal structure. The shallow potential well associated with the 10th vibrational mode indicates that the weakly bonded Cs atoms would rattle from their equilibrium positions under minimal perturbations. We further calculated the atom displacement parameters (ADPs) of Cs and Te atoms, as shown in Fig. S5 of the SM. The results clearly show that the ADPs of Cs atoms are considerably larger than those of Te atoms, indicating that Cs atoms are loosely bound within the lattice. The rattling phonon modes were frequently observed in material with weakly bonded single or multiple atoms.[27,28] To quantify the interatomic interaction strength, we calculate the interatomic force constants (IFCs) for the nearest X-I (X = Cs, Te) atomic pairs. The results show that the IFC for Cs-I atomic pairs is 0.14 eV/Å^2, far smaller than the 3.34 eV/Å^2 obtained for Te-I pairs, indicating that the interaction between Cs and I atoms is significantly weaker than that between Te and I atoms. This significant difference in IFCs indicates a pronounced bonding hierarchy in Cs_2TeI_6, consequently impeding phonon propagation.[29] In the frequency range corresponding to Cs atom vibrations, the calculated phonon scattering rate and phonon group velocity, as shown in the highlighted region in Fig. S4 of the SM, indicate that rattling atoms cause a significant scattering rate and a small group velocity. Specifically, the weakly bonded Cs atoms act as phonon scattering centers, while the strongly bonded Te atoms provide a smooth conduct channel for phonon transmission.

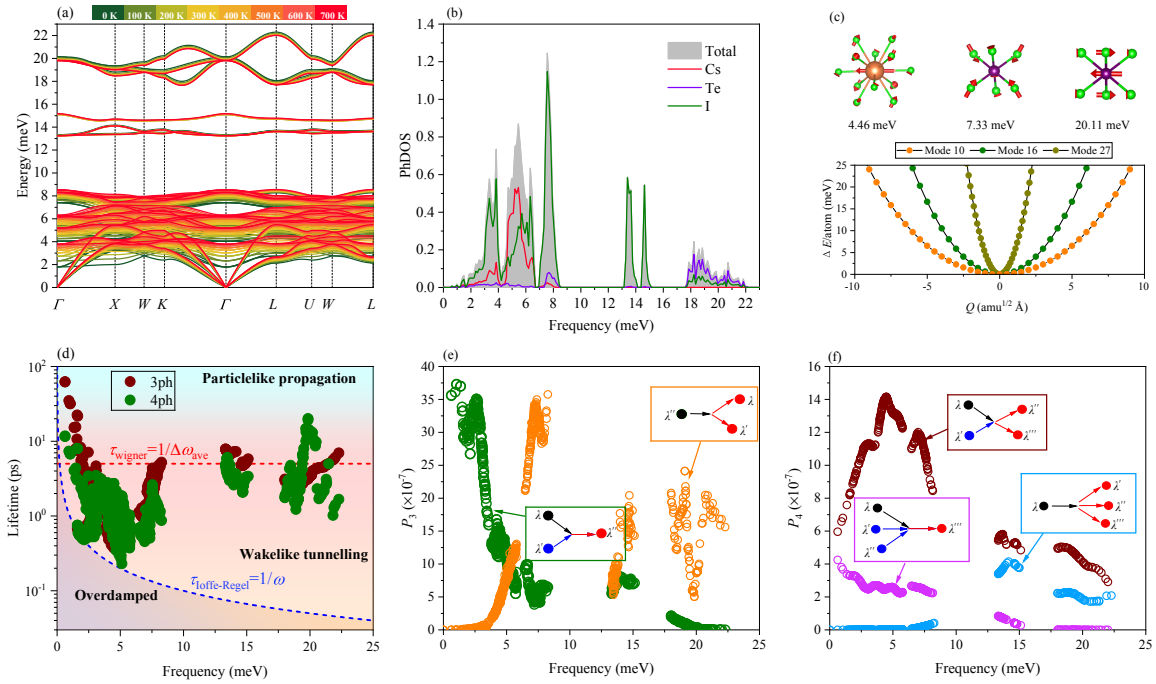

Fig. 2. (a) Calculated phonon dispersion relations along high symmetry directions at different temperatures. (b) Atom-projected PhDOS at 300 K. (c) Potential energies of three optical modes at Γ point as a funciton of the corresponding nomal-mode coordinates. The corresponding vibration frequencies and vibrational modes are shown in the figure. (d) Calculated intrinsic 3ph (maroon dots) and 4ph (green dots) lifetimes as a function of frequency at 300 K. (e) Decomposed 3ph weighted phase space for combining ($\lambda+\lambda'=\lambda''$) and splitting ($\lambda''=\lambda+\lambda'$) processes. (f) Decomposed 4ph weighted phase space for splitting ($\lambda=\lambda'+\lambda''+\lambda'''$), redistribution ($\lambda+\lambda'=\lambda''+\lambda'''$), and combination ($\lambda+\lambda'+\lambda''=\lambda'''$) processes.

To assess the impact of bonding hierarchy on the lattice dynamical properties, we further calculate the Grüneisen parameter (γ) as a function of frequency, as shown in Fig. S4(b) of the SM. A pronouncedly large value of γ is observed at the vibrational frequency corresponding to the Cs atoms, indicating that the rattling of Cs atoms does enhance the anharmonic phonon–phonon scattering. The total γ, derived from the longitudinal and transverse sound velocities, is 1.91 for Cs_2TeI_6. These characteristics suggest that the bonding hierarchy potentially leads to strong anharmonicity.

Next, we analyze the phonon scattering mechanisms. In Fig. 2(d), we present our calculated the three-phonon (3ph) and the four-phonon (4ph) lifetimes at temperature of 300 K. We observe that the 3ph lifetimes exceed those of the 4ph processes across a broad frequency range. However, the 4ph lifetimes become more dominant at higher frequencies (around 20 meV). This indicates that the 3ph interaction serves as the dominant scattering mechanism, while the 4ph scattering also plays a non-negligible role in enhancing the scattering of the high-frequency optical phonons. To evaluate the contributions of the particle-like and the wavelike conduction mechanisms, we marked the Wigner limit τ_{Wigner} and the Ioffe–Regel limit $\tau_{\text{Ioffe–Regel}}$ in Fig. 2(d). In Cs_2TeI_6, incorporating the 4ph interactions substantially increases the proportion of the phonon modes in the wavelike tunneling regime compared to considering only the 3ph processes. Consequently, a significant population of phonons falls within the $\tau_{\text{Ioffe–Regel}} < \tau < \tau_{\text{Wigner}}$ range, indicating a substantial κ_c contribution to the total κ_L.

To gain a deeper understanding of the 3ph and 4ph scattering processes, we analyze the phase space for them as presented in Figs. 2(e) and 2(f), respectively. Obviously, the 3ph scattering processes can be categorized into splitting ($\lambda''=\lambda+\lambda'$) and combination ($\lambda+\lambda'=\lambda''$) processes. The splitting process exhibits an increased phase space with the increasing frequency, while the combination process demonstrates a decreasing trend. The 4ph scattering processes can be categorized into three distinct processes, splitting ($\lambda=\lambda'+\lambda''+\lambda'''$), redistribution ($\lambda+\lambda'=\lambda''+\lambda'''$), and combination ($\lambda+\lambda'+\lambda''=\lambda'''$). Notably, the redistribution process plays a dominant role in the 4ph scattering. The scattering phase spaces of all the three subprocsses are significantly reduced due to the anharmonic corrections.

We estimate the κ_L by solving the Boltzmann transport equation (BTE) within the relaxation-time approximation,[30] as implemented in modified FOURPHONON packages.[31–33] Figure 3(a) presents the temperature-dependent κ_L from 300 to 700 K, exploring the 4ph effect and the off-diagonal contributions of κ_c. At 300 K, the κ_p is approximately 0.2 $W{\cdot}m^{-1}{\cdot}K^{-1}$ when considering only the 3ph scattering. As expected, incorporating the 4ph interactions results in an approximately 50% reduction in κ_p, indicating that the 4ph scattering plays a significant role in diminishing κ_p. Conversely, incorporating the 4ph interactions leads to an increase in κ_c and a stronger temperature dependence compared to considering only the 3ph interactions. This phenomenon is mainly

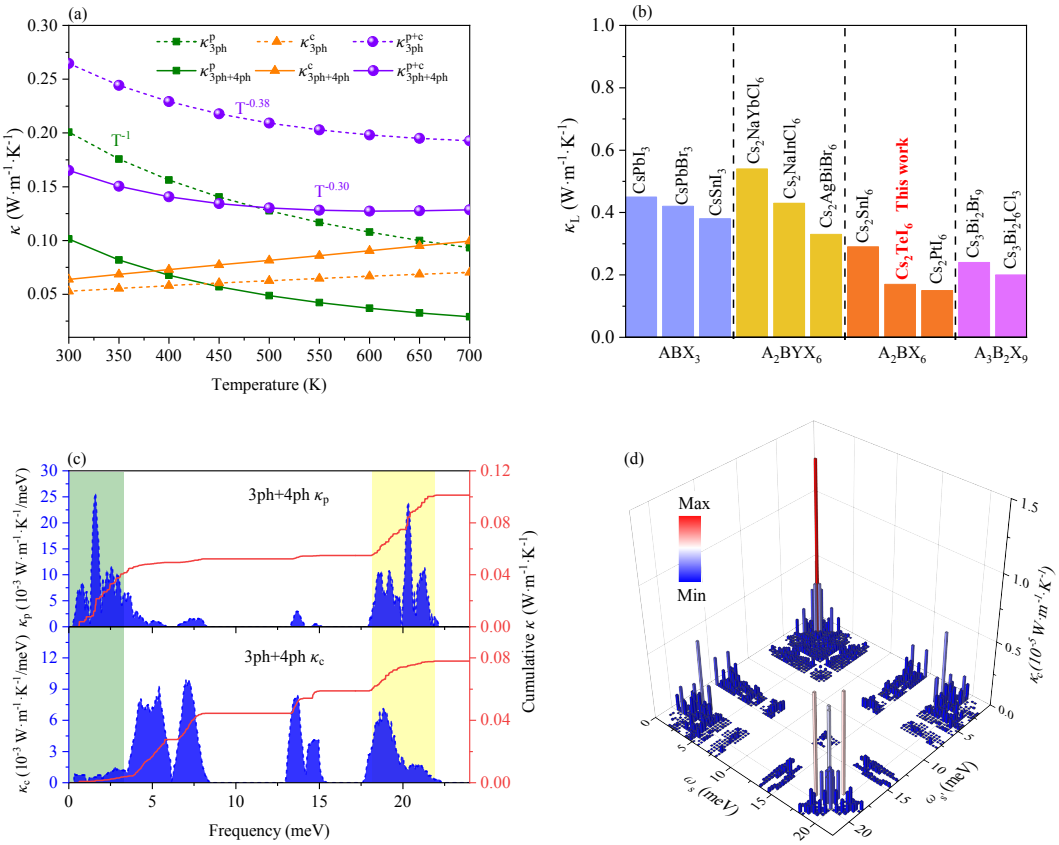

Fig. 3. (a) Calculated κ_L of Cs_2TeI_6 including the 3ph and 4ph as a function of temperature. The κ_p and κ_c are the particle-like and wavelike contributions, respectively. (b) Room-temperature κ_L for Cs_2TeI_6 in comparison with that reported for other all-inorganic halide perovskites.[8,37,42–48] (c) Thermal conductivity spectra and cumulative lattice thermal conductivity of κ_p and κ_c for Cs_2TeI_6 as a function of frequency at 300 K. (d) Three-dimensional stacked bar plots of the off-diagonal terms contributing to κ_c in Cs_2TeI_6 versus the frequency of different phonon pairs.

due to the fact that the 4ph interactions yield a scattering rate $\Gamma^{4ph}_{q,s} \approx \omega^4 T^2$, while the 3ph interactions yield $\Gamma^{3ph}_{q,s} \approx \omega^2 T$.[29,34] The increased temperature sensitivity of κ_c with the 4ph underscores its increasingly significant role in κ_L, especially at higher temperatures. Therefore, the 4ph interactions are non-negligible in Cs_2TeI_6 and are crucial for accurately describing the wavelike contribution to the total κ_L. Unlike the T^{-1} trend of the κ_p, the total κ_L, when incorporating the wavelike contribution, shows a weaker temperature dependence of $T^{-0.38}$ and $T^{-0.30}$ by including the 3ph and 3ph+4ph scattering, respectively. Similar behaviors have also been observed in several highly anharmonic crystals.[29,35–37] Considering κ_c, the total κ_L of Cs_2TeI_6 is 0.17 W·m^{-1}·K^{-1} at 300 K. This is lower than the typical TE materials such as PbTe ($\kappa_L \sim 2.00$ W·m^{-1}·K^{-1})[38,39] and SnSe ($\kappa_L \sim 0.67$ W·m^{-1}·K^{-1}),[40] and comparable to recently reported ultralow κ_L systems, including $CsAg_5Te_3$ (0.18 W·m^{-1}·K^{-1})[41] and $Bi_4O_4SeCl_2$ ($\kappa_L \sim 0.1$ W·m^{-1}·K^{-1}).[42] Figure 3(b) compares the κ_L of Cs_2TeI_6 with other halide perovskite families (ABX_3, A_2BYX_6, and $A_3B_2X_9$),[8,37,43–49] which generally show low κ_L. Notably, the vacancy-ordered double perovskite systems of Cs_2TeI_6 and Cs_2PtI_6[46] exhibit even lower κ_L than others.

To understand the origin of the ultralow κ_L in Cs_2TeI_6, we calculate the thermal conductivity spectra and its cumulative values of κ_p and κ_c as a function of frequency at 300 K, as shown in Fig. 3(c). In this figure, the green-shaded region represents the contribution of the acoustic branches to κ_L, while the yellow-shaded region represents the contribution of the high-frequency optical branches. We find that in addition to the acoustic branches, the high-frequency optical modes also contribute significantly to the κ_p. Typically, acoustic branches are considered the dominant contributors to the κ_L in most materials. Optical phonon-dominated heat transport is observed in fewer materials, such as SnS[50] and $BaSnS_2$,[51] where the optical branches exhibit relatively high phonon group velocities. As shown in Fig. S4(a) of the SM, the high-frequency optical branches of Cs_2TeI_6 also display elevated phonon group velocities. Moreover, upon accounting for the 4ph interactions, the lifetimes of these high-frequency optical branches exhibit significant extension. These factors collectively lead to a substantial contribution of the high-frequency optical branches to the κ_L. To further substantiate this observation, we calculate the contributions of individual phonon modes to the κ_p, considering both the 3ph and the combined 3ph+4ph scattering processes, as shown in Fig. S6 of the SM. Given the significant role of the opti-

cal branches, we classify modes 4–9 as low-frequency optical branches (OPT_l), modes 10–24 as mid-frequency optical branches (OPT_m) and modes 25–27 as high-frequency optical branches (OPT_h). Notably, the optical modes make a significant contribution to κ_p, where the OPT_h are particularly dominant. This dominance mainly stems from the large phonon gap and the pronounced dispersion characteristic of the OPT_h. Furthermore, when the 4ph scattering is included, the contribution from the acoustic branches increases markedly, while the relative contribution of the optical modes correspondingly decreases. This behavior reflects the differing responses of the acoustic and the optical branches to the 4ph scattering. From the visualization of the vibrational modes at Γ, we observe that the high-frequency optical modes are associated with the Te-dominated vibrations of the $[TeI_6]^{2-}$ octahedra. The vibrational directions of the Te atoms oppose those of the I atoms. Our bond strength analysis reveals that the Te-I bonds are notably strong, potentially providing a smooth conduit for phonon transmission. To verify the significant impact of the bonding hierarchy on thermal conductivity, we artificially reduce the strength of the second-order IFCs of the I-Te pairs by 50% using a toy model.[52–54] Compared with the actual phonon dispersion shown in Fig. S7 of the SM, the low-frequency phonon dispersions in the toy model exhibit significant hardening, implying that a reduced bonding hierarchy leads to increased phonon group velocities. Additionally, we find that as the Te-I bond strength decreases, the total γ drops from 1.91 to 1.77, indicating that the bonding hierarchy is responsible for the strong lattice anharmonicity.

Conversely, κ_c is primarily attributed to the optical branches, while the acoustic modes contribute relatively small, as indicated by the green-shaded region in Fig. 3(c). To understand the off-diagonal coupling of the vibrational eigenstates in Cs_2TeI_6, we calculate the resolved κ_c in terms of the coupled mode frequencies ω_s, $\omega_{s'}$ at 300 K, as shown in Fig. 3(d). The phonon pairs that contribute most significantly to the κ_c are primarily distributed along the quasi-diagonal regions ($\omega_s \approx \omega_{s'}$) due to the smaller energy difference between eigenstates. Furthermore, phonon pairs in the non-diagonal regions also contribute to κ_c at high-frequency region. It is evident that the non-negligible contribution of these modes can be attributed to their high group velocities, which stem from the obvious broadening of the high-frequency phonons.

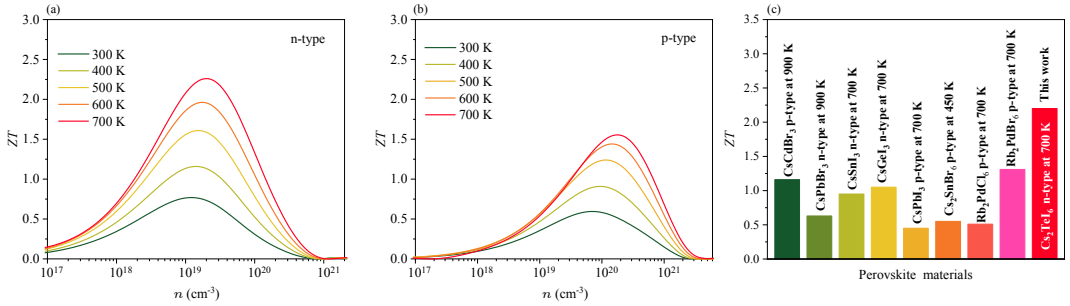

Fig. 4. Predicted ZT values for (a) n-type and (b) p-type Cs_2TeI_6 as a function of temperature and carrier concentration. (c) Comparison between the ZT of Cs_2TeI_6 and reported TE materials with typical perovskite systems.[56–60]

Motivated by its ultralow κ_L, we predict that the Cs_2TeI_6 is a promising TE material. The electronic transport properties are calculated using the electron BTE as implemented in the AMSET code.[55] The band structures of Cs_2TeI_6 without and with spin–orbit coupling (SOC) are shown in Fig. S8 of the SM. The inclusion of SOC modifies the electronic structures, leading to a reduction in band gap and a splitting of the conduction bands. Consequently, SOC has been incorporated into the calculation of the TE properties. Figure S9 of the SM presents the Seebeck coefficients (S), electrical conductivity (σ), power factor ($PF = S^2\sigma$), and the electronic thermal conductivity (κ_e) at various temperature as a function of carrier concentration n for n-type and p-type Cs_2TeI_6. The ZT values for n-type and p-type Cs_2TeI_6 at different temperatures are shown in Figs. 4(a) and 4(b), respectively. As can be seen, the ZT values for n-type doping are notably higher than those for p-type doping. The highest ZT values of 2.26 for n-type doping is observed at 700 K. For p-type doping, the highest ZT value is 1.56 at 700 K, achieved at an optimized carrier concentration of 1.8×10^{20} cm^{-3}. Therefore, Cs_2TeI_6 is a promising n-type TE material. Motivated by the exceptionally low κ_L observed in typical perovskites systems, recent studies have explored the TE performance of various perovskites. While some predicted TE properties show deviations from experimental measurements, comparisons with existing literature indicate that the calculated ZT values remain reasonably consistent. Figure 4(c) highlights the promising ZT values achieved by both existing literature[56–60] and this work. Consequently, we conclude that with optimized carrier concentrations, Cs_2TeI_6 exhibits superior TE performance compared to other perovskites.

In summary, we systematically explored the TE properties of Cs_2TeI_6, employing a combination of first-principles calculation, BTE, and unified phonon-transport theory. We found that its ultralow κ_L can be attributed to the special bonding hierarchy, which induces the partially localized vibrations and strong anharmonicity. The 4ph can induce strong phonon scattering rates, driving the

heat transfer from the particle-like phonon propagation to the wavelike phonon tunneling transport. By incorporating both the 4ph interactions and the phonon coherence, the n-type ZT values can reach 2.26 at 700 K, making it comparable to the most excellent TE materials. Our study will stimulate further experimental and theoretical investigations of halide perovskites in the fields of TE materials and anharmonic phonon dynamics.

Acknowledgements. This work was supported by the National Natural Science Foundation of China (Grant Nos. 12204482 and U2330104), the Scientific and Technological Innovation Programs of Higher Education Institutions in Shanxi (Grant No. 2020L0537), the Natural Science Foundation of Shanxi Province (Grant No. 202403021221164), Higher Education Teaching Reform and Innovation Project of Shanxi Province (Grant No. J20220480), and Graduate Curriculum Ideological and Political Education Project of Shanxi Normal University (Grant No. 010520233013).

References

[1] Qin B, Kanatzidis M G, and Zhao L D 2024 *Science* **386** eadp2444
[2] Gong Y, Dou W, Lu B, Zhang X, Zhu H, Ying P, Zhang Q, Liu Y, Li Y, Huang X, Iqbal M F, Zhang S, Li D, Zhang Y, Wu H, and Tang G 2024 *Nat. Commun.* **15** 4231
[3] Ren J 2023 *Chin. Phys. Lett.* **40** 090501
[4] Wang S F, Zhang Z G, Wang B T, Zhang J R, and Wang F W 2021 *Chin. Phys. Lett.* **38** 046301
[5] Wu G, Cai J, Chen L, Guo Z, Chen K, Tan X, Wu J, Liu G Q, and Jiang J 2024 *Adv. Funct. Mater.* **34** 2407818
[6] Cho H, Back S Y, Sato N, Liu Z, Gao W, Wang L, Nguyen H D, Kawamoto N, and Mori T 2024 *Adv. Funct. Mater.* **34** 2407017
[7] Acharyya P, Ghosh T, Pal K, Rana K S, Dutta M, Swain D, Etter M, Soni A, Waghmare U V, and Biswas K 2022 *Nat. Commun.* **13** 1
[8] Bhui A, Ghosh T, Pal K, Singh Rana K, Kundu K, Soni A, and Biswas K 2022 *Chem. Mater.* **34** 3301
[9] Xie Q Y, Xiao F, Tang Z Y, Zhang K W, and Wang B T 2025 *Phys. Rev. B* **111** 024302
[10] Haque M A, Kee S, Villalva D R, Ong W L, and Baran D 2020 *Adv. Sci.* **7** 1903389
[11] Liu W, Jie Q, Kim H S, and Ren Z 2015 *Acta Mater.* **87** 357
[12] Zhou Y, Wang J, Luo D, Hu D, Min Y, and Xue Q 2022 *Nano Energy* **94** 106949
[13] Xu F, Zhang M, Li Z, Yang X, and Zhu R 2023 *Adv. Energy Mater.* **13** 2203911
[14] Ghorui S, Kangsabanik J, Aslam M, and Alam A 2024 *Phys. Rev. Appl.* **21** 024036
[15] Vazquez-Fernandez I, Mariotti S, Hutter O S, Birkett M, Veal T D, Hobson T D, Phillips L J, Danos L, Nayak P K, Snaith H J, Xie W, Sherburne M P, Asta M, and Durose K 2020 *Chem. Mater.* **32** 6676
[16] Padelkar S S, Vikram, Jasieniak J J, Simonov A N, and Alam A 2024 *Phys. Rev. Appl.* **21** 044031
[17] Pal B, Kale A J, Sharma M, Bhamu K, Kang S G, Singh V K, and Dixit A 2024 *Energy Fuels* **38** 1430
[18] Huang Q, Tian C, Lai J, Qi F, Zhang N, Liu J, Liang Z, Wu D, and Tang X 2022 *Inorg. Chem.* **61** 14447
[19] Maughan A E, Ganose A M, Bordelon M M, Miller E M, Scanlon D O, and Neilson J R 2016 *J. Am. Chem. Soc.* **138** 8453
[20] Ma J J, Zheng J J, Chen Y, Ren Q, Zhang J, and Wang B T 2024 *Phys. Chem. Chem. Phys.* **26** 21801
[21] Bhumla P, Jain M, Sheoran S, and Bhattacharya S 2022 *J. Phys. Chem. Lett.* **13** 11655
[22] Mouhat F and Coudert F X 2014 *Phys. Rev. B* **90** 224104
[23] Wei B, Zhang X, Li W, Li J, Li Y, Gao Q, Hong J, Nan C W, and Lin Y H 2025 *Appl. Phys. Rev.* **12** 011324
[24] Christensen M, Abrahamsen A B, Christensen N B, Juranyi F, Andersen N H, Lefmann K, Andreasson J, Bahl C R H, and Iversen B B 2008 *Nat. Mater.* **7** 811
[25] Zhang T and Zhu L 2024 *J. Mater. Chem. C* **12** 15578
[26] Rana K S, Nidhi, Bera C, Biswas K, and Soni A 2024 *J. Mater. Chem. A* **12** 22756
[27] Ghosh T, Dutta M, Sarkar D, and Biswas K 2022 *J. Am. Chem. Soc.* **144** 10099
[28] Dhivya M C N, Mohamed J K P, Archana J, and Navaneethan M 2025 *Appl. Phys. Lett.* **126** 154102
[29] Dutta M, Sarkar D, and Biswas K 2021 *Chem. Commun.* **57** 4751
[30] Tadano T and Tsuneyuki S 2018 *Phys. Rev. Lett.* **120** 105901
[31] Li W, Carrete J, Katcho N A, and Mingo N 2014 *Comput. Phys. Commun.* **185** 1747
[32] Han Z, Yang X, Li W, Feng T, and Ruan X 2022 *Comput. Phys. Commun.* **270** 108179
[33] Ji L, Huang A, Huo Y, Ding Y M, Zeng S, Wu Y, and Zhou L 2024 *Phys. Rev. B* **109** 214307
[34] Feng T, Lindsay L, and Ruan X 2017 *Phys. Rev. B* **96** 161201
[35] Kukreti S, Ramawat S, and Dixit A 2024 *Phys. Rev. B* **109** 205203
[36] Liu P F, Li X, Li J, Zhu J, Tong Z, Kofu M, Nirei M, Xu J, Yin W, Wang F, Liang T, Xie L, Zhang Y, Singh D J, Ma J, Lin H, Zhang J, He J, and Wang B T 2024 *Natl. Sci. Rev.* **11** nwae216
[37] Wang G, Zheng J, Xue J, Xu Y, Zheng Q, Hautier G, Lu H, and Zhou Y 2024 *Adv. Sci.* **12** 2408149
[38] El-Sharkawy A A, EI-Azm A M, Kenawy M, Hillal A S, and Abu-Basha H M 1983 *Int. J. Thermophys.* **4** 261
[39] Tian Z, Garg J, Esfarjani K, Shiga T, Shiomi J, and Chen G 2012 *Phys. Rev. B* **85** 184303
[40] Zhao L D, Lo S H, Zhang Y, Sun H, Tan G, Uher C, Wolverton C, Dravid V P, and Kanatzidis M G 2014 *Nature* **508** 373
[41] Lin H, Tan G, Shen J N, Hao S, Wu L M, Calta N, Malliakas C, Wang S, Uher C, Wolverton C, and Kanatzidis M G 2016 *Angew. Chem.* **128** 11603
[42] Gibson Q D, Zhao T, Daniels L M, Walker H C, Daou R, Hebert S, Zanella M, Dyer M S, Claridge J B, and Slater B *et al.* 2021 *Science* **373** 1017
[43] Lee W, Li H, Wong A B, and Yang P 2017 *Proc. Natl. Acad. Sci.* **114** 8693
[44] Cappai A, Melis C, Marongiu D, Quochi F, Saba M, Congiu F, He Y, Slade T J, Kanatzidis M G, and Colombo L 2024 *Adv. Sci.* **11** 2305861
[45] Klarbring J, Hellman O, Abrikosov I A, and Simak S I 2020 *Phys. Rev. Lett.* **125** 045701
[46] Sajjad M, Mahmood Q, Singh N, and Larsson J A 2020 *ACS Appl. Energy Mater.* **3** 11293
[47] Chen X, Zhou J, Luo J, Zhang J, Qiu P, and Shi X 2024 *Small* **20** 2405276
[48] Acharyya P, Ghosh T, Pal K, Rana K S, Dutta M, Swain D, Etter M, Soni A, Waghmare U V, and Biswas K 2022 *Nat. Commun.* **13** 5053
[49] Klarbring J, Hellman O, Abrikosov I A, and Simak S I 2020 *Phys. Rev. Lett.* **125** 045701
[50] Guo R, Wang X, Kuang Y, and Huang B 2015 *Phys. Rev. B* **92** 115202
[51] Li Z, Xie H, Hao S, Xia Y, Su X, Kanatzidis M G, Wolverton C, and Tang X 2021 *Phys. Rev. B* **104** 245209
[52] Ji J, Liu Z, Dai J, Qiu D, Yang J, Xi J, Long Y, and Zhang W 2023 *Mater. Today Phys.* **32** 101005

[53] Ding J, Lanigan-Atkins T, Calderón-Cueva M, Banerjee A, Abernathy D L, Said A, Zevalkink A, and Delaire O 2021 *Sci. Adv.* **7** eabg1449
[54] Wu Y, Ji J, Ding Y, Yang J, and Zhou L 2024 *Adv. Sci.* **11** 2406380
[55] Ganose A M, Park J, Faghaninia A, Woods-Robinson R, Persson K A, and Jain A 2021 *Nat. Commun.* **12** 1
[56] Shang W, Hu T, Li D, Li S, Zhou X, Feng C, and Li D 2024 *J. Electron. Mater.* **53** 4512
[57] Yao Z, Cao W, Wang Z, Miao L, Shi J, and Xiong R 2023 *Phys. Chem. Chem. Phys.* **25** 26236
[58] Jong U G, Kim Y S, Ri C H, Kye Y H, and Yu C J 2021 *J. Phys. Chem. C* **125** 6013
[59] Zeng X, Jiang J, Niu G, Sui L, Zhang Y, Wang X, Liu X, Chen A, Jin M, and Yuan K 2022 *J. Phys. Chem. Lett.* **13** 9736
[60] Liu R, Hu Y, Feng C, Ding G, Zhang G, and Li D 2023 *ChemNanoMat* **9** e202200450